Supporting Information

Enhanced Water Splitting for Hydrogen Production via Z-Scheme Heterostructures of Mo@CTF-0, HfS_2, and HfSSe Monolayers

Qing-Guo Sun [a], Chuan-Lu Yang[a,c,*], Xiaohu Li[b,c], Yuliang Liu[a], Wenkai Zhao[a], and Feng Gao[d]

[a] *School of Physics and Optoelectronic Engineering, Ludong University, Yantai, 264025, China*

[b] *Xinjiang Astronomical Observatory, Chinese Academy of Science, Urumqi 830011, China*

[c] *Key Laboratory of Radio Astronomy, Chinese Academy of Science, Urumqi 830011, China*

[d] *Department of Physics, Southern University and A&M College, LA70813, United States*

1. The geometrical configurations and electronic properties of the monolayers and their heterostructures.

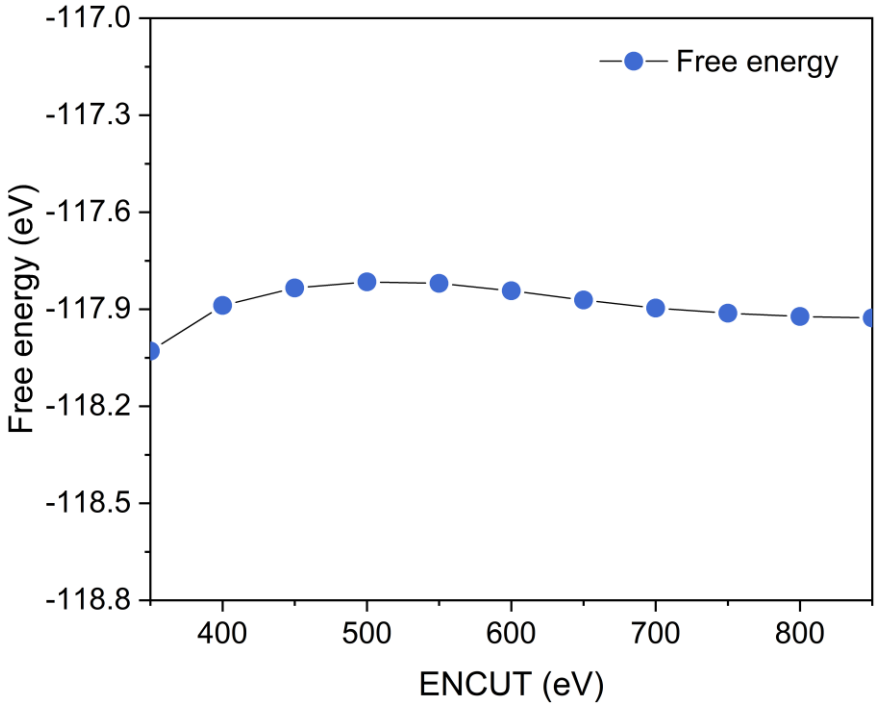

Fig. S1. The convergence test results of the cutoff energy for the CTF-0 monolayer.

*Corresponding author. *E-mail address:* ycl@ldu.edu.cn. (C.L. Yang).

Table S1. The lattice constants (a), bond length of C-N (R), band gaps (E_g), energies of the CBM and VBM and over potentials (χ) of the monolayers.

Monolayers	a (Å)	R (Å)	E_g (eV)	E_{CBM}	E_{VBM}	$\chi(H_2)/\chi(O_2)$ (eV)
Ti@CTF-0	7.37	2.05	0.75	-1.96	-2.70	1.74/-
Zr@CTF-0	7.38	2.18	0.17	-1.91	-2.08	3.08/-
Hf@CTF-0	7.36	2.23	0.58	-2.29	-2.87	1.88/-
Cr@CTF-0	7.36	2.00	2.36	-1.37	-3.73	2.84/-
Mo@CTF-0	7.36	2.14	1.60	-1.53	-3.13	2.64/-
W@CTF-0	7.36	2.14	0.78	-2.11	-2.89	2.02/-
Ru@CTF-0	7.32	2.22	0.99	-1.83	-2.82	1.77/-
Os@CTF-0	7.33	2.22	0.64	-2.10	-2.74	1.49/-
Pd@CTF-0	7.30	2.57	2.32	-1.77	-4.09	1.57/-
Pt@CTF-0	7.25	2.00	2.20	-2.11	-4.31	1.45/-
HfS_2	3.61	-	1.98	-1.79	-3.77	-/1.30
HfSSe	3.68	-	1.40	-1.75	-3.15	-/0.65

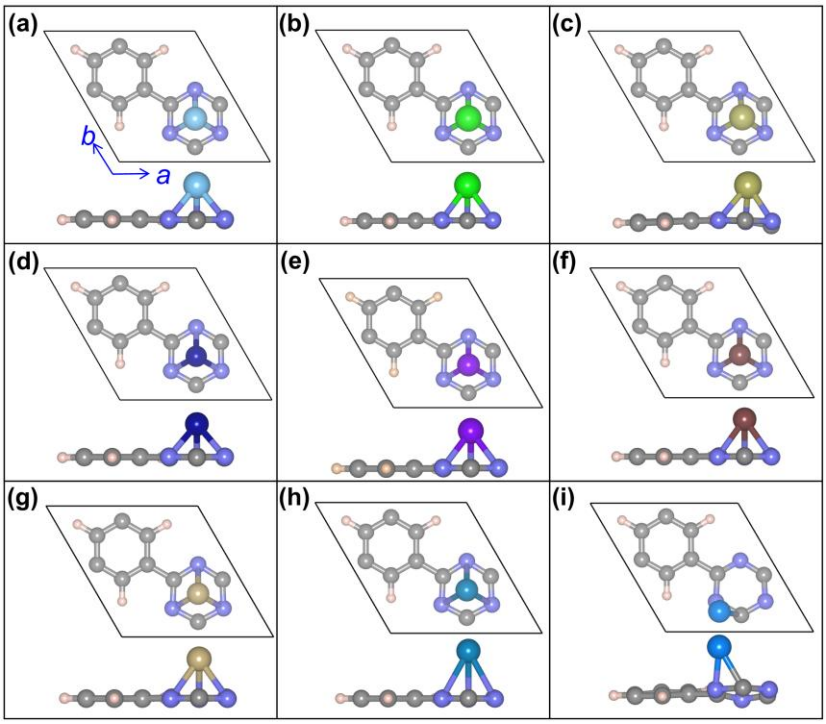

Fig. S2. The optimized structures for the considered monolayers. (a) Ti@CTF-0, (b) Zr@CTF-0, (c) Hf@CTF-0, (d) Cr@CTF-0, (e) W@CTF-0, (f) Ru@CTF-0, (g) Os@CTF-0, (h) Pd@CTF-0 and Pt@CTF-0 monolayers.

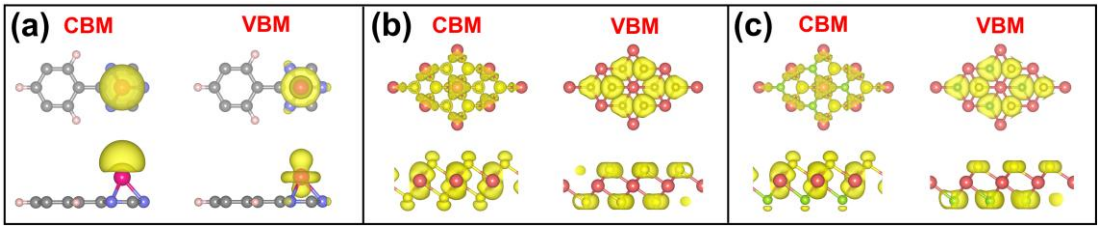

Fig. S3. Partial charge populations of CBMs and VBMs for the (a) Mo@CTF-0, (b) HfS_2 and (c) HfSSe monolayers.

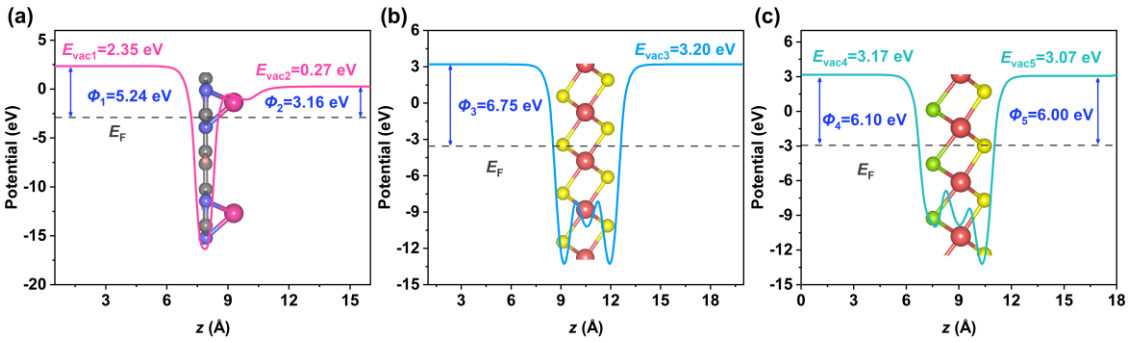

Fig. S4. The static potential curves. (a), (b) and (c) for the Mo@CTF-0, HfS_2 and HfSSe monolayers.

Table S2. The lattice constants (a), interlayer distance (d), and formation energy (E_f) of the Mo@CTF-0/HfS_2-based configurations.

Configurations	a (Å)	d (Å)	E_f (meV/Å^2)
MD	7.30	3.33	-11.50
MD_x	7.30	3.33	-11.27
MD_y	7.30	3.38	-11.37
M_xD	7.26	2.24	-93.32
M_xD_x	7.29	2.53	-93.75
M_xD_y	7.25	2.46	-102.82
M_yD	7.30	3.36	-11.49
M_yD_x	7.30	3.32	-11.66
M_yD_y	7.30	3.34	-11.20

Table S3. The lattice constants (a), interlayer distance (d), and formation energy (E_f) of the Mo@CTF-0/α-HfSSe-based configurations.

Configurations	a (Å)	d (Å)	E_f (meV/Å²)
ME	7.34	3.34	-12.39
ME_x	7.35	3.40	-13.01
ME_y	7.35	3.40	-12.26
M_xE	7.30	2.47	-95.26
M_xE_x	7.31	2.57	-89.76
M_xE_y	7.29	2.46	-104.40
M_yE	7.35	3.36	-12.09
M_yE_x	7.35	3.38	-13.50
M_yE_y	7.34	3.34	-12.07

Table S4. The lattice constants (a), interlayer distance (d), and formation energy (E_f) of the Mo@CTF-0/β-HfSSe-based configurations.

Configurations	a (Å)	d (Å)	E_f (meV/Å²)
ME′	7.34	3.40	-13.32
ME'_x	7.34	3.35	-12.14
ME'_y	7.35	3.43	-13.08
M_xE'	7.32	2.58	-82.91
$M_xE'_x$	7.34	2.34	-52.39
$M_xE'_y$	7.31	2.57	-91.05
M_yE'	7.35	3.42	-12.99
$M_yE'_x$	7.34	3.33	-12.57
$M_yE'_y$	7.35	3.40	-12.95

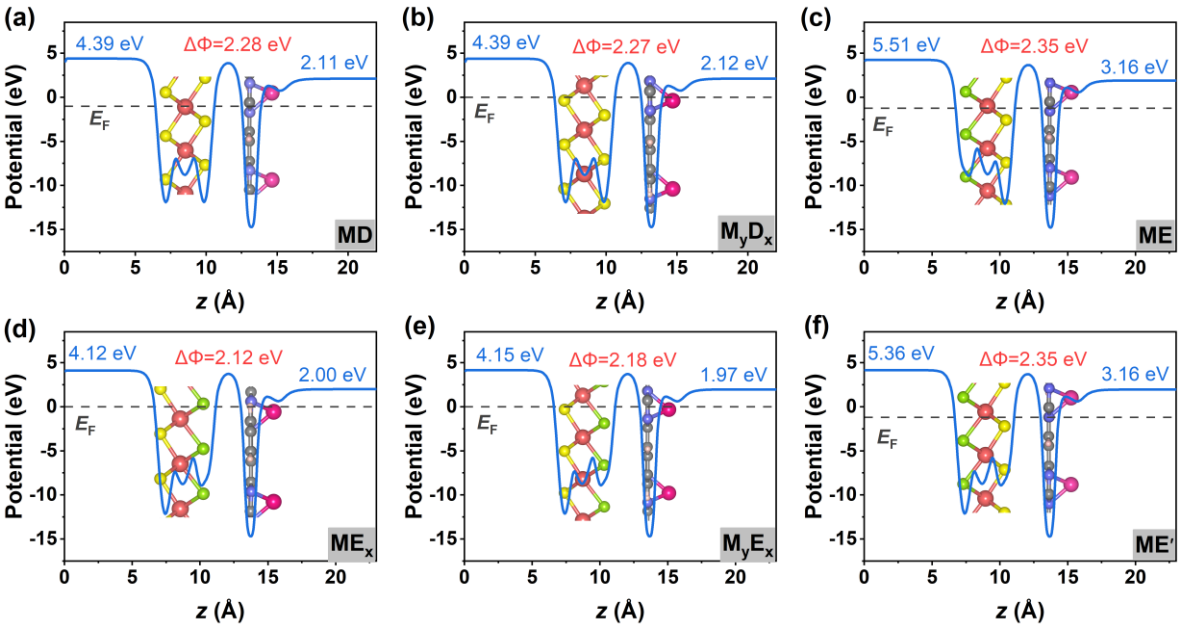

Fig. S5. The static potential curves for the six configurations.

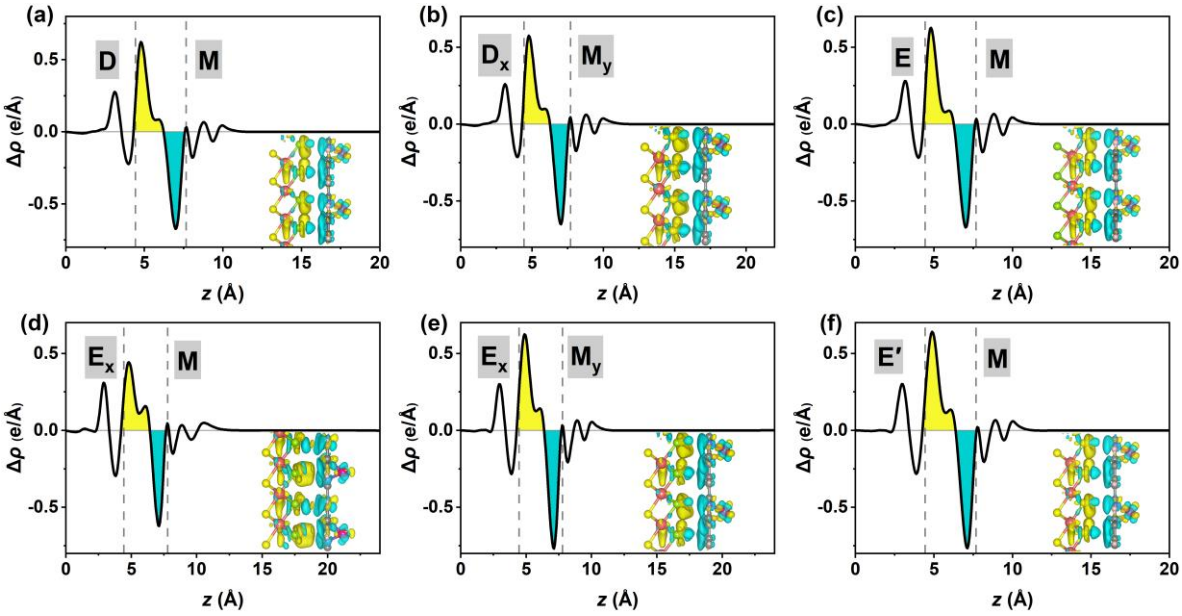

Fig. S6. Differential charge density distributions of the six configurations.

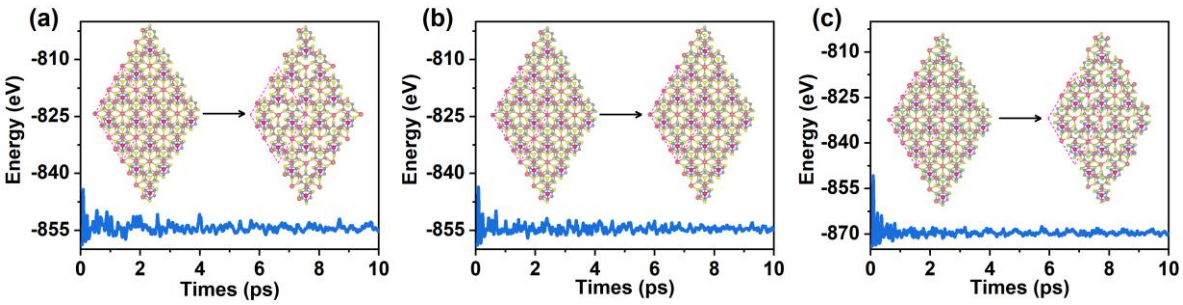

Fig. S7. The AIMD simulation results in a temperature of 300 K for the considered structures. (a) Mo@CTF-0/HfS_2, (b) Mo@CTF-0/α-HfSSe and (C) Mo@CTF-0/β-HfSSe heterostructures.

2. Calculational details for the solar-to hydrogen conversion efficiency (η'_{STH}) and the optical properties.

The equation of optical absorption coefficient $\alpha(\omega)$ is

$$\alpha(\omega) = \sqrt{2}\sqrt{\sqrt{\varepsilon_r^2(\omega) + \varepsilon_i^2}(\omega) - \varepsilon_r(\omega)} \quad (1)$$

Where $\varepsilon_i(\omega)$ is the imaginary part of the complex dielectric function $\varepsilon(\omega) = \varepsilon_r(\omega) + i\varepsilon_i(w)$, can be calculated by the following equation:[1]

$$\varepsilon_{\mathrm{i}}(\omega) = \frac{4\pi^2}{m^2\omega^2}\Sigma_{\mathrm{c,v}}\int_{BZ}\frac{2}{(2\pi)^3}|M_{\mathrm{c,v}}(k)|^2\delta(\varepsilon_{\mathrm{ck}} - \varepsilon_{\mathrm{vk}} - h_\omega)d^3k \quad (2)$$

Where $|Mc,\ v(k)|^2$ represent the momentum matrix element, and c and v represent the conduction and valence band states, respectively. $\varepsilon_i(\omega)$ can be calculated by VASP. The real part $\varepsilon_r(\omega)$ can be calculated from the imaginary part $\varepsilon_i(\omega)$ of the complex dielectric function by using the Kramer-Kroning relationship.[2]

The solar-to-hydrogen conversion efficiency (η_{STH}) is the result of the efficiency of light absorption η_{abs} and the efficiency of carrier utilization η_{cu}, which can be considered a crucial factor in determining the catalytic ability of photocatalysts. We calculated η_{STH}, η_{abs}, and η_{cu}

based on the following formula[3]

$$\eta_{\mathrm{STH}} = \eta_{\mathrm{abs}} \times \eta_{\mathrm{cu}} \tag{3}$$

$$\eta_{\mathrm{abs}} = \frac{\int_{E_g}^{\infty} P(\hbar\omega)d(\hbar\omega)}{\int_{0}^{\infty} P(\hbar\omega)d(\hbar\omega)} \tag{4}$$

$$\eta_{\mathrm{cu}} = \frac{\Delta G \int_{E}^{\infty} \frac{P(\hbar\omega)}{\hbar\omega} d(\hbar\omega)}{\int_{E_{\mathrm{g}}}^{\infty} P(\hbar\omega)d(\hbar\omega)} \tag{5}$$

$$E = \begin{cases} E_{\mathrm{g}}, (\chi(H_2) \geq 0.2, \chi(O_2) \leq 0.6) \\ E_{\mathrm{g}} + 0.2 - \chi(\mathrm{H_2}), (\chi(\mathrm{H_2}) < 0.2, \chi(0_2) \geq 0.6) \\ E_{\mathrm{g}} + 0.6 - \chi(O_2), (\chi(\mathrm{H_2}) \geq 0.2, \chi(O_2) < 0.6) \\ E_{\mathrm{g}} + 0.8 - \chi(\mathrm{H_2}) - \chi(O_2), (\chi(\mathrm{H_2}) < 0.2, \chi(O_2) < 0.6) \end{cases} \tag{6}$$

Where $P(\hbar\omega)$ is the AM1.5G solar energy flux at the photo energy; E_{g} (HSE) is the bandgap of the layer materials; $\chi(\mathrm{H_2})$ and $\chi(\mathrm{O_2})$ are the overpotentials for hydrogen and oxygen evolution reactions, respectively. ΔG represents the potential difference of 1.23 eV for water splitting, and E is the energy of photons that can actually be utilized for water splitting. Because the intrinsic electric field would promote the electron-hole separation, so the corrected STH efficiency (η'_{STH}) for polarized materials in photocatalytic water splitting reaction can be calculated as:

$$\eta'_{\mathrm{STH}} = \eta_{\mathrm{STH}} \times \frac{\int_{0}^{\infty} P(\hbar\omega)\mathrm{d}(\hbar\omega)}{\int_{0}^{\infty} P(\hbar\omega)\mathrm{d}(\hbar\omega) + \Delta\Phi \int_{0}^{\infty} P(\hbar\omega)\mathrm{d}(\hbar\omega)} \tag{7}$$

Where $\Delta\Phi$ is the work function difference between the two surfaces of the polarized material. It is worth noting that in a heterostructure, the photoexcitation process occurs within the monolayers composing the heterostructure. Therefore, the η'_{STH} is limited by the bandgap value of the monolayer with the larger bandgap in the heterostructure. Consequently, when calculating the η'_{STH} of a heterostructure, the E_{g} value in the formula (4), (5), and (6) should

be the bandgap value of the monolayer with the larger bandgap after forming the heterostructure.

Table S5. The overpotentials, bandgaps, work function differences (ΔΦ), and the corrected STH efficiency of the six configurations.

Configurations	$\chi(H_2)$, $\chi(O_2)$ (eV)	$E_{g\text{-}M}$, $E_{g\text{-}D/E}$ (eV)	ΔΦ (eV)	η'_{STH} (%)
MD	2.65, 1.39	1.57, 2.13	2.28	11.76
M_yD_x	2.65, 1.40	1.58, 2.14	2.27	10.73
ME	2.64, 0.69	1.59, 1.44	2.34	20.18
ME_x	2.64, 0.58	1.60, 1.42	2.12	19.42
M_yE_x	2.65, 0.59	1.60, 1.44	2.19	19.47
ME′	2.65, 0.60	1.60, 1.44	2.20	20.36

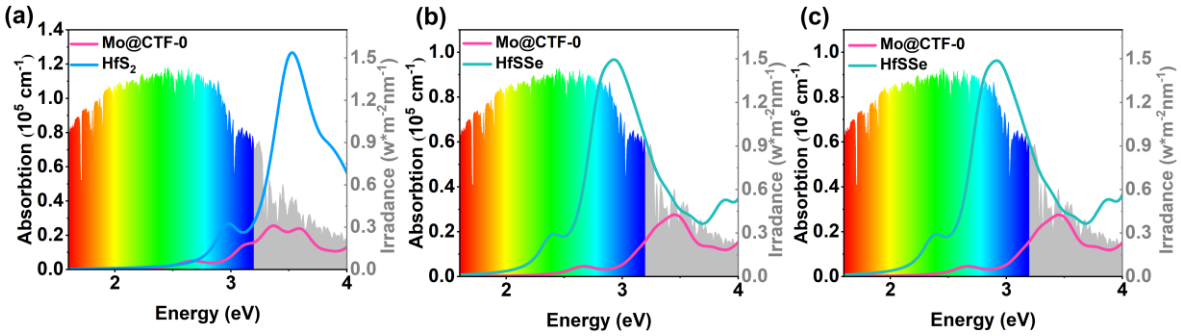

Fig. S8. The optical absorption coefficients. (a), (b) and (c) for the Mo@CTF-0/HfS_2, Mo@CTF-0/*α*-HfSSe and Mo@CTF-0/*β*-HfSSe heterostructures, respectively.

Table S6. The overpotentials (χ), bandgaps of HfS_2 (E_{g1}) and Mo@CTF-0 (E_{g2}) and work function differences ($\Delta\Phi$), energy conversion efficiency of the light absorption of light (η_{abs}), carrier utilization (η_{cu}), and η'_{STH} of the HfS_2/Mo@CTF-0 heterostructure.

Strain	$\chi(H_2)$, $\chi(O_2)$ (eV)	E_{g1}, E_{g2} (eV)	$\Delta\Phi$ (eV)	η_{abs} (%)	η_{cu} (%)	η_{STH} (%)	η'_{STH} (%)
-4%	2.66, 1.06	1.76, 1.34	2.35	49.69	52.54	26.11	17.42
-3%	2.66, 1.16	1.87, 1.40	2.34	44.12	50.61	22.33	15.67
-2%	2.66, 1.24	1.96, 1.46	2.32	39.69	49.09	19.48	14.25
-1%	2.65, 1.32	2.06, 1.52	2.29	35.14	47.52	16.70	12.74
0	2.65, 1.39	2.13, 1.57	2.28	32.32	46.54	15.04	11.76
1%	2.64, 1.46	2.21, 1.62	2.26	29.16	45.44	13.25	10.65
2%	2.64, 1.53	2.28, 1.68	2.25	26.40	44.46	11.74	9.66
3%	2.63, 1.58	2.34, 1.73	2.22	24.26	43.69	10.60	8.90
4%	2.62, 1.63	2.38, 1.77	2.20	22.90	43.19	9.89	8.40

Table S7. The overpotentials (χ), bandgaps of HfSSe (E_{g1}) and Mo@CTF-0 (E_{g2}) and work function differences ($\Delta\Phi$), energy conversion efficiency of the light absorption of light (η_{abs}), carrier utilization (η_{cu}), and η'_{STH} of the SeHfS/Mo@CTF-0 heterostructure.

Strain	$\chi(H_2)$, $\chi(O_2)$ (eV)	E_{g1}, E_{g2} (eV)	$\Delta\Phi$ (eV)	η_{abs} (%)	η_{cu} (%)	η_{STH} (%)	η'_{STH} (%)
-4%	2.67, 0.27	0.95, 1.38	2.46	70.54	39.60	27.94	15.09
-3%	2.66, 0.37	1.08, 1.43	2.42	67.59	44.08	29.79	16.67
-2%	2.66, 0.48	1.20, 1.49	2.40	64.03	49.43	31.65	18.38
-1%	2.65, 0.56	1.30, 1.54	2.37	61.37	53.70	32.95	19.72
0	2.64, 0.69	1.44, 1.59	2.34	58.37	55.65	32.49	20.18
1%	2.65, 0.77	1.53, 1.65	2.33	55.45	54.58	30.27	19.24
2%	2.63, 0.85	1.61, 1.69	2.31	53.18	53.77	28.59	18.60
3%	2.64, 0.93	1.69, 1.76	2.29	49.69	52.54	26.11	17.57
4%	2.62, 0.99	1.76, 1.80	2.26	47.62	51.82	24.68	16.98

Table S8. The overpotentials (χ), bandgaps of HfSSe (E_{g1}) and Mo@CTF-0 (E_{g2}) and work function differences ($\Delta\Phi$), energy conversion efficiency of the light absorption of light (η_{abs}), carrier utilization (η_{cu}), and η'_{STH} of the SHfSe/Mo@CTF-0 heterostructure.

Strain	$\chi(H_2)$, $\chi(O_2)$ (eV)	E_{g1}, E_{g2} (eV)	$\Delta\Phi$ (eV)	η_{abs} (%)	η_{cu} (%)	η_{STH} (%)	η'_{STH} (%)
-4%	2.67, 0.14	0.95, 1.37	2.25	71.06	33.31	23.67	13.24
-3%	2.66, 0.25	1.07, 1.44	2.23	66.70	37.34	25.02	14.58
-2%	2.66, 0.34	1.17, 1.49	2.22	64.03	41.36	26.48	15.88
-1%	2.66, 0.41	1.35, 1.55	2.11	60.70	44.25	26.86	16.91
0	2.65, 0.60	1.44, 1.60	2.20	57.77	55.53	32.02	20.36
1%	2.68, 0.69	1.54, 1.70	2.18	52.71	53.60	28.25	18.83
2%	2.64, 0.77	1.62, 1.71	2.17	52.27	53.45	27.94	18.71
3%	2.63, 0.86	1.70, 1.76	2.16	49.69	52.54	26.11	17.90
4%	2.62, 0.93	1.78, 1.80	2.14	47.62	51.82	24.68	17.27

3. Details and calculational results of the carrier mobility.

The carrier mobilities of the monolayers were calculated using the deformation potential (DP) theory.[4] The equation is[5-7]

$$\mu = \frac{2e\hbar^3 C}{3k_B T|m^*|^2 E_d^2} \quad (8)$$

where the carrier mobility μ depends on the elastic modulus C, effective mass m^*, and deformation potential constant E_d. e, h, k_B, and T are the electron charge, the reduced Planck constant, the Boltzmann constant, and temperature. C, m^*, E_d, defined as $C = \frac{1}{S_0}\frac{\partial^2 E}{\partial \varepsilon^2}$, $\frac{1}{m^*} = \frac{1}{\hbar}\frac{\partial^2 E(k)}{\partial k^2}$ and $E_d = \frac{\partial E_{edge}}{\partial \varepsilon}$, respectively. Here, ε is the ratio of lattice parameter under the uniaxial strain along x or y direction on the rectangle cell, E is the total energy of the monolayer under uniaxial strains, S_0 is the area of the monolayer, and E(k) is the energy

corresponding to k, k is the wavevector. E_{edge} is the energy of the band edge positions calculated by HSE06. The detailed results are shown in Figs. S9-S12.

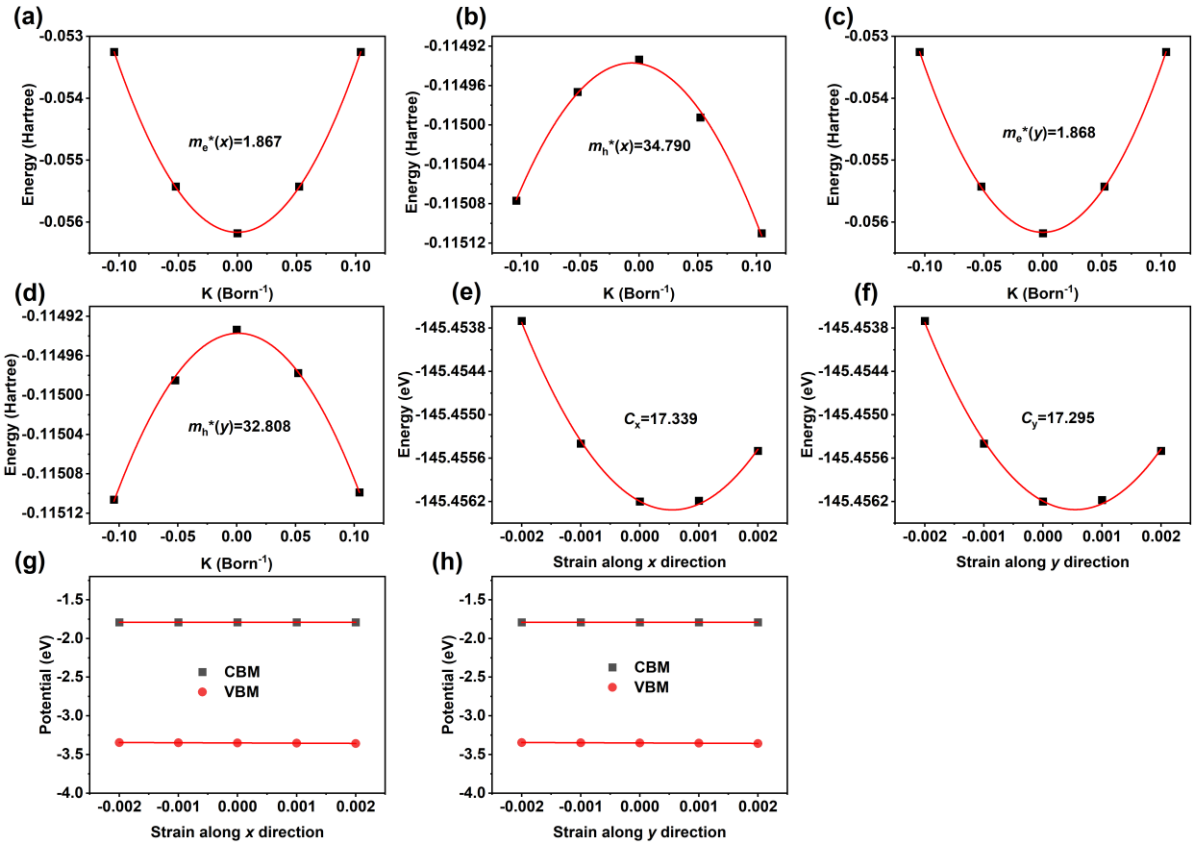

Fig. S9. Fitting curve of elastic constant (C), deformation potential constant (E_d), and effective mass (m^*) of the Mo@CTF-0 monolayer. (a) and (b) are the m^* fitting curves of the electrons along the x and y directions, respectively. (c) and (d) are the m^* fitting curves of the holes along the x and y directions, respectively. (e) and (f) are the fitting curves of C along the x and y directions, respectively. (g) and (h) are the fitting curves of E_d along the x and y directions, respectively.

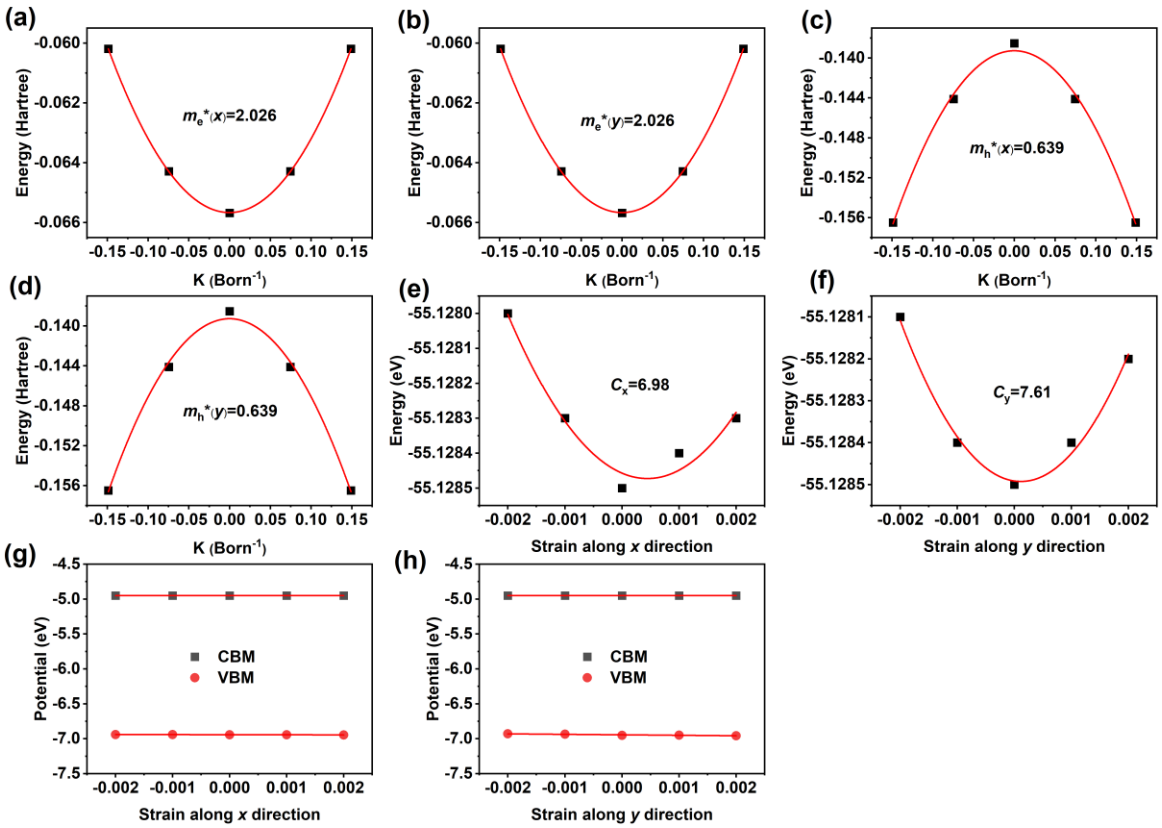

Fig. S10. Fitting curve of elastic constant (C), deformation potential constant (E_d), and effective mass (m*) of the HfS_2 monolayer. (a) and (b) are the m* fitting curves of the electrons along the x and y directions, respectively. (c) and (d) are the m* fitting curves of the holes along the x and y directions, respectively. (e) and (f) are the fitting curves of C along the x and y directions, respectively. (g) and (h) are the fitting curves of E_d along the x and y directions, respectively.

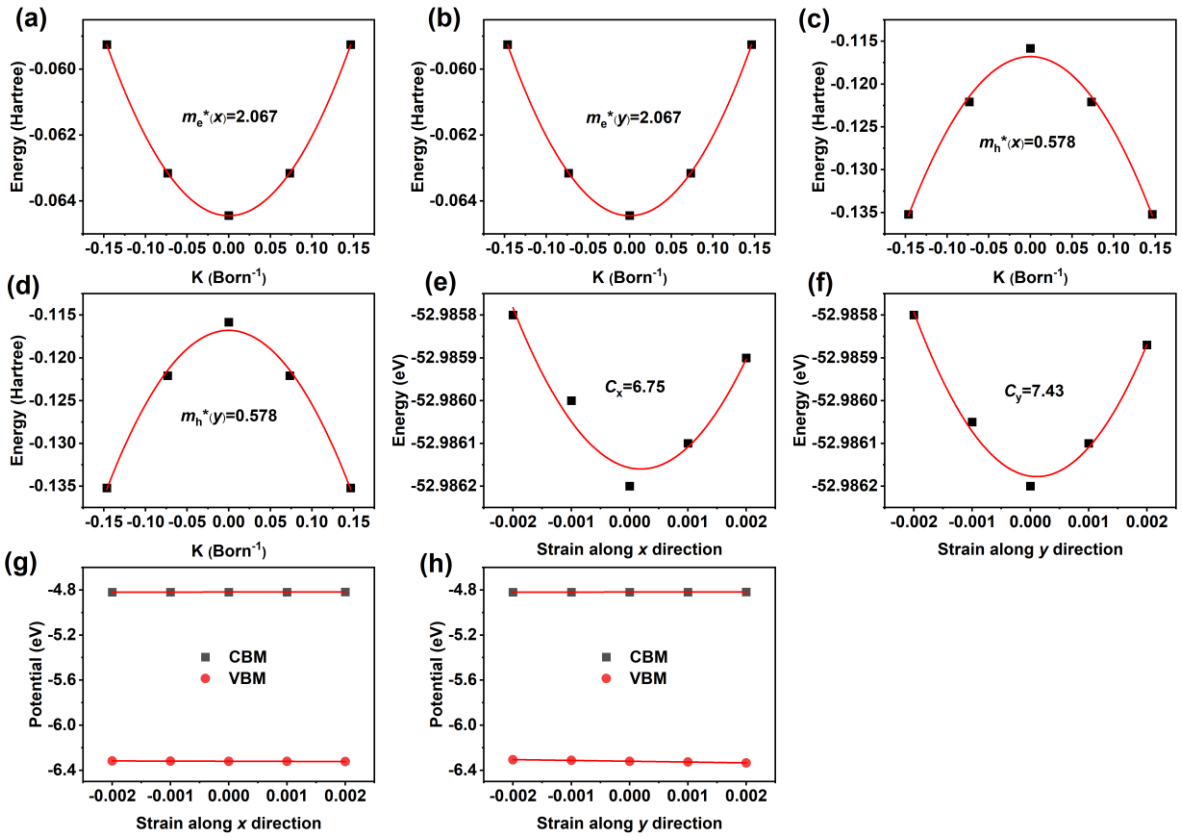

Fig. S11. Fitting curve of elastic constant (C), deformation potential constant (E_d), and effective mass (m^*) of HfSSe monolayer. (a) and (b) are the m^* fitting curves of the electrons along the x and y directions, respectively. (c) and (d) are the m^* fitting curves of the holes along the x and y directions, respectively. (e) and (f) are the fitting curves of C along the x and y directions, respectively. (g) and (h) are the fitting curves of E_d along the x and y directions, respectively.

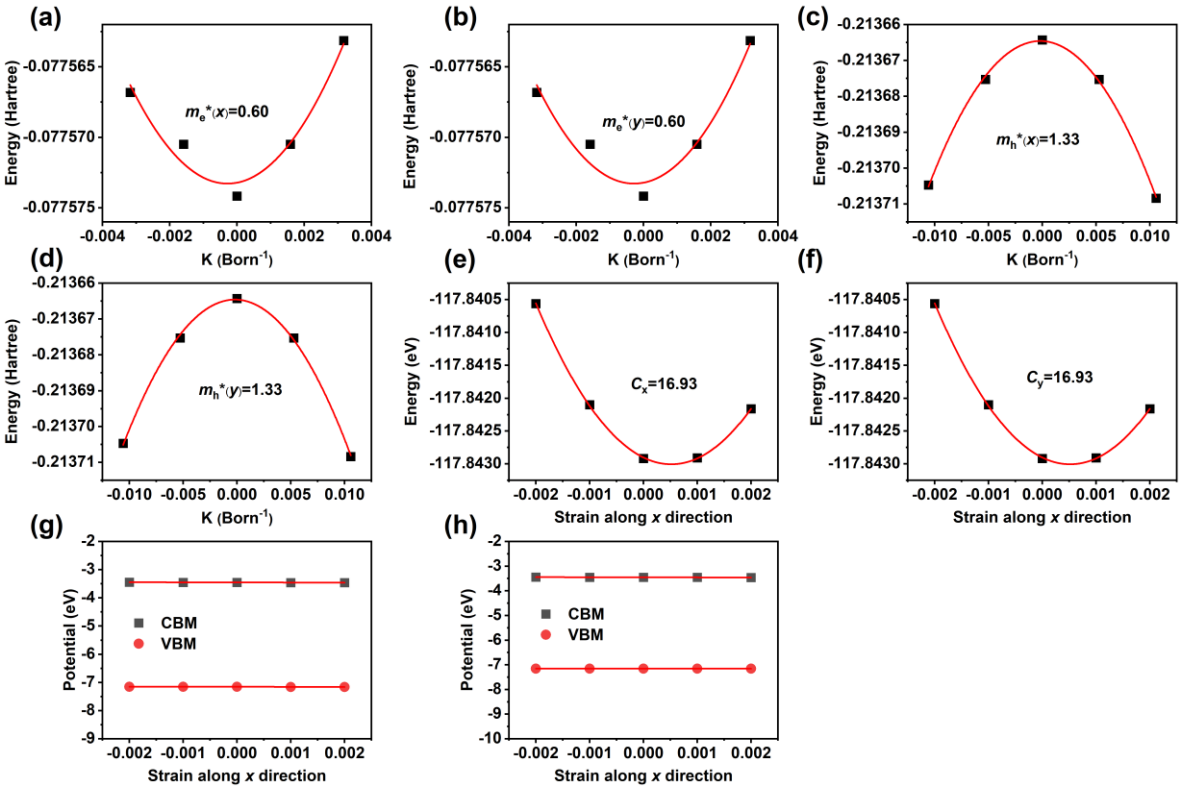

Fig. S12. Fitting curve of elastic constant (C), deformation potential constant (E_d), and effective mass (m^*) of CTF-0 monolayer. (a) and (b) are the m^* fitting curves of the electrons along the x and y directions, respectively. (c) and (d) are the m^* fitting curves of the holes along the x and y directions, respectively. (e) and (f) are the fitting curves of C along the x and y directions, respectively. (g) and (h) are the fitting curves of E_d along the x and y directions, respectively.

Table S9. The elastic modulus (C), deformation potential constant (E), and carrier mobility (μ) for the Mo@CTF-0, HfS_2, HfSSe and CTF-0 monolayers at 300 K.

Monolayer	direction	m_e/m_h	E_e/E_h (eV)	C (Jm^{-2})	μ_e/μ_h ($cm^2 V^{-1} S^{-1}$)
Mo@CTF-0	x	1.87/34.79	0.28/2.91	286.09	14433.56/0.38
	y	1.87/32.81	0.26/2.89	285.37	16679.16/0.44
HfS_2	x	2.03/0.64	0.20/1.30	115.17	9670.98/2301.02
	y	2.03/0.64	0.30/6.71	125.57	4686.16/94.45
HfSSe	x	2.07/0.58	0.20/1.30	111.38	8984.98/2719.67
	y	2.07/0.58	0.20/7.21	122.60	9890.13/97.59
CTF-0	x	0.60/1.33	3.48/0.71	279.35	883.39/4316.08
	y	0.60/1.33	3.48/0.71	279.35	883.39/4319.08

4. Calculational method of the Gibbs free energy.

The ΔG can be calculated by the following equation:[8]

$$\Delta G = \Delta E - T\Delta S - \Delta E_{\mathrm{ZPE}} \quad (9)$$

Where ΔE, ΔE_{ZPE} and ΔS represent the differences in total energy, zero-point energy, and entropy of the slab with and without adsorbed intermediates. T is the temperature 298 K. The E_{ZPE} can be calculated by E_{ZPE} =1/2 $\Sigma \hbar\nu$, where the ν is the vibrational frequency over normal modes, and the zero-point of the slab can be negligible. The entropies of the free molecules were taken from the standard tables in Physical chemistry and those of intermediates were obtained from vibrational frequency. For those reactions involving the release of protons and electrons, the free energy of one pair of proton and electron (H^+/e^-) was taken as $1/2G_{H_2}$.

In the aqueous solution, the HER with two electrons pathway, which can be written as:

$$* + H^+ + e^- \rightarrow *H$$

$$*H + H^+ + e^- \rightarrow * + H_2$$

The single site pathway of the OER process can be written as:

$$H_2O + * \rightarrow *OH + H^+ + e^-$$

$$*OH \rightarrow *O + H^+ + e^-$$

$$*O + H_2O \rightarrow *OOH + H^+ + e^-$$

$$*OOH \rightarrow * + O_2 + H^+ + e^-$$

The free energy change for HER step can be expressed as:

$$\Delta G_{H*} = G_{H*} - 1/2G_{H_2} - G_*$$

The free energy changes for OER steps can be expressed as:

$$\Delta G_1 = G_{OH*} + 1/2G_{H_2} - G_{H_2O} - G_*$$

$$\Delta G_2 = G_{O*} + 1/2G_{H_2} - G_{OH*}$$

$$\Delta G_3 = G_{OOH*} + 1/2G_{H_2} - G_{H_2O} - G_{O*}$$

$$\Delta G_4 = G_{O_2} + G_* - G_{OOH*}$$

Table S10. Gibbs free energy changes for OER in heterostructures.

Heterostructures	ΔG_1 (eV)	ΔG_2 (eV)	ΔG_3 (eV)	ΔG_4 (eV)
Mo@CTF-0/HfS_2	2.23	0.55	2.89	-0.75
Mo@CTF-0/α-HfSSe	2.34	1.02	2.03	-0.47
Mo@CTF-0/β-HfSSe	2.19	0.59	2.65	-0.51

5. Calculational details of the NAMD simulation.

The nonadiabatic molecular dynamics (NAMD) simulation for the carrier transfer and the electron-hole recombination were carried out by Hefei-NAMD code.[9]

The fluctuations are characterized by the energy gap autocorrelation function (ACF) which defined by[10]

$$C_{(t)} = \frac{\langle \delta U(t)\delta U(t_0)\rangle_T}{\langle (\delta U(t_0))^2\rangle_T} = \frac{C_{un}(t)}{\langle \Delta E^2(0)\rangle_T} \quad (10)$$

δU is the deviation of the energy gap from the average value, $C_{un}(t)$ is the unnormalized ACF, $C_{(t)}$ is the normalized ACF.[11]

$$\delta U(t) = \Delta E_{ij}(\mathbf{R}(t)) - \langle \Delta E_{ij}(\mathbf{R}(t))\rangle_T \quad (11)$$

The ΔE_{ij} is the energy difference between the i and j states, and **R**(t) is determined through the quantum force.

$$D(t) = exp\left[-\frac{\langle (\delta U)^2\rangle_T}{\hbar^2}\int_0^t d\tau_2 \int_0^{\tau_2} d\tau_1 C(\tau_1)\right] \quad (12)$$

The spectral density was calculated by applying the Fourier transform of an ACF function.[12]

$$I(\omega) = \left|\frac{1}{\sqrt{2\pi}}\int_{-\infty}^{+\infty} dt e^{-i\omega t} C(t)\right|^2 \quad (13)$$

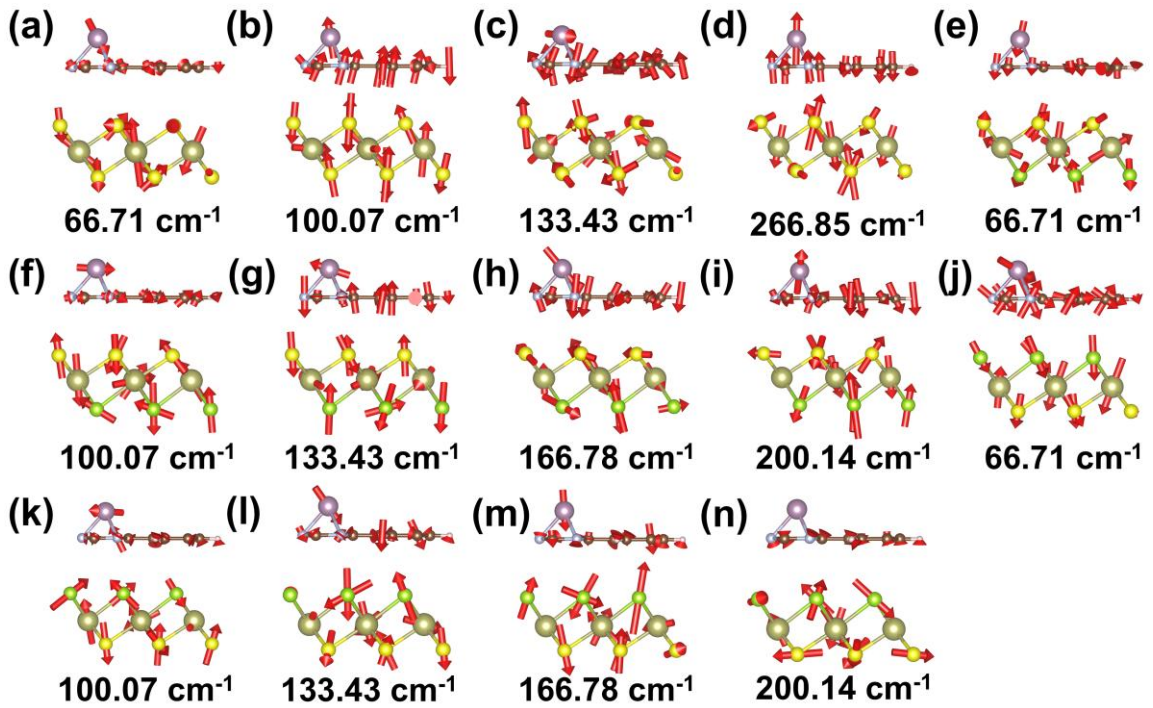

Fig. S13. The vibration modes of (a)-(d) Mo@CTF-0/HfS_2, (e)-(i) Mo@CTF-0/α-HfSSe and (j)-(n) Mo@CTF-0/β-HfSSe.

6. References.

1 Li, P. *et al.* First-principle study of optical properties of Cu-doped CdS. *Opt. Commun.* **295**, 45-52 (2013). https://doi.org:https://doi.org/10.1016/j.optcom.2012.12.086

2 Li, Y. & Chen, Z. Tuning Electronic Properties of Germanane Layers by External Electric Field and Biaxial Tensile Strain: A Computational Study. *The Journal of Physical Chemistry C* **118**, 1148-1154 (2014). https://doi.org:10.1021/jp411783q

3 Fu, C.-F. *et al.* Intrinsic Electric Fields in Two-dimensional Materials Boost the Solar-to-Hydrogen Efficiency for Photocatalytic Water Splitting. *Nano Lett.* **18**, 6312-6317 (2018). https://doi.org:10.1021/acs.nanolett.8b02561

4 Gao, W. *et al.* Vacancy-defect modulated pathway of photoreduction of CO2 on single atomically thin AgInP2S6 sheets into olefiant gas. *Nat. Commun.* **12**, 4747 (2021). https://doi.org:10.1038/s41467-021-25068-7

5 Bruzzone, S. & Fiori, G. Ab-initio simulations of deformation potentials and electron mobility in chemically modified graphene and two-dimensional hexagonal boron-nitride. *Appl. Phys. Lett.* **99** (2011). https://doi.org:10.1063/1.3665183

6 Chen, J., Xi, J., Wang, D. & Shuai, Z. Carrier Mobility in Graphyne Should Be Even Larger than That in Graphene: A Theoretical Prediction. *The Journal of Physical Chemistry Letters* **4**, 1443-1448 (2013). https://doi.org:10.1021/jz4005587

7 Dai, J. & Zeng, X. C. Titanium Trisulfide Monolayer: Theoretical Prediction of a New Direct-Gap Semiconductor with High and Anisotropic Carrier Mobility. *Angewandte Chemie International Edition* **54**, 7572-7576 (2015). https://doi.org:https://doi.org/10.1002/anie.201502107

8 Gao, G., O'Mullane, A. P. & Du, A. 2D MXenes: A New Family of Promising Catalysts for the Hydrogen Evolution Reaction. *ACS Catalysis* **7**, 494-500 (2017). https://doi.org:10.1021/acscatal.6b02754

9 Zheng, Q. *et al.* Ab initio nonadiabatic molecular dynamics investigations on the excited carriers in condensed matter systems. *WIREs Computational Molecular Science* **9**, e1411 (2019). https://doi.org:https://doi.org/10.1002/wcms.1411

10 Long, R. & Prezhdo, O. V. Quantum Coherence Facilitates Efficient Charge Separation at a MoS2/MoSe2 van der Waals Junction. *Nano Lett.* **16**, 1996-2003 (2016). https://doi.org:10.1021/acs.nanolett.5b05264

11 Jaeger, H. M., Fischer, S. & Prezhdo, O. V. Decoherence-induced surface hopping. *The Journal of Chemical Physics* **137** (2012). https://doi.org:10.1063/1.4757100

12 Bardeen, J. & Shockley, W. Deformation Potentials and Mobilities in Non-Polar Crystals. *Physical Review* **80**, 72-80 (1950). https://doi.org:10.1103/PhysRev.80.72